Energy &
Environmental
Science

PAPER

View Article Online
View Journal | View Issue

Cite this: *Energy Environ. Sci.*, 2016, **9**, 2152

High-energy-density lithium-ion battery using a carbon-nanotube–Si composite anode and a compositionally graded $Li[Ni_{0.85}Co_{0.05}Mn_{0.10}]O_2$ cathode†

Joo Hyeong Lee,‡[a] Chong S. Yoon,‡[b] Jang-Yeon Hwang,[a] Sung-Jin Kim,[c] Filippo Maglia,[c] Peter Lamp,[c] Seung-Taek Myung[d] and Yang-Kook Sun*[a]

Received 18th April 2016,
Accepted 20th May 2016

DOI: 10.1039/c6ee01134a

www.rsc.org/ees

A fully operational practical Li-rechargeable battery system delivering unprecedented high energy density with excellent cycle life was proposed using the state-of-the-art cathode and anode technologies. Based on the simple ball-milling process, a carbon nanotube (CNT)–Si composite anode with extremely stable long-term cycling, while providing a discharge capacity of 2364 mA h g^{-1} at a tap density of 1.103 g cm^{-3}, was developed. For the cathode, a two-sloped full concentration gradient (TSFCG) $Li[Ni_{0.85}Co_{0.05}Mn_{0.10}]O_2$ cathode, designed to obtain maximum possible discharge capacity by having a Ni-enriched core and to simultaneously ensure high chemical and thermal stability by having an outer Mn-enriched layer, yielded a discharge capacity of 221 mA h g^{-1}. Integrating the CNT–Si composite and the TSFCG cathode in a full cell configuration, the full cell generated an energy density of 350 W h kg^{-1} with excellent capacity retention for 500 cycles at 1 C rate, satisfying the energy density limit imposed by the drive range requirement for EVs. The proposed battery system satisfied the demands for energy storage for vehicle applications in terms of energy density, power and cycle life.

1. Introduction

Lithium ion batteries (LIBs) have the highest gravimetric and volumetric energy densities among the commercialized batteries that can provide electric drives for plug-in hybrid (PHEVs) and fully electric vehicles (EVs). Despite the increasing utilization of the LIBs, the share of electric vehicles in the world's automotive market has been growing at a slower rate than expected.[1] The cost-to-range ratio can often be identified as one of the primary factors responsible for the slow growth. A driving range of at least 300 miles is typically considered to be the threshold to guarantee the success of future electric vehicles.[2] The drive range requirement translates into an energy density of *ca.* 100 W h kg^{-1}, which requires the current LIB packs to be increased by a factor of 2.5. Although clever cell design and improvements in cell subcomponents can bear potential for volume and weight reduction, major developments in high capacity cathode and anode active materials are essential.[3] $Li[Ni_{0.8}Co_{0.1}Mn_{0.1}]O_2$ (NCM) and $Li[Ni_{0.8}Co_{0.15}Al_{0.05}]O_2$ (NCA) in particular are the most promising candidates for EVs among the next-generation of high energy density cells owing to their high capacity, outstanding rate capability, and low cost. Despite the advantages, increasing the Ni fraction in the NCM cathodes negatively impacts the lifetime and safety of the battery, particularly when higher cut-off voltages and high electrode packing densities are pursued.[4] A number of strategies have been explored to increase the stability of the Ni-enriched NCM cathode material by suppressing the parasitic side reactions with the electrolyte. Among them, a compositionally graded cathode material in which concentrations of the transition metals continuously varied from the particle center to the surface appears to be the most promising since the graded cathodes have demonstrated remarkable improvements over cathodes with single uniform composition, not only in lifetime and safety, but also in battery power due to the superior Li^+ diffusion kinetics.[5–9] However, like conventional NCM cathodes, it is challenging to increase the Ni concentration above 80% even in the compositionally graded NCM cathodes; hence, a NCM cathode that is compositionally graded with multi-level gradients was introduced

---

[a] *Department of Energy Engineering, Hanyang University, Seoul 133-791, Republic of Korea. E-mail: yksun@hanyang.ac.kr*
[b] *Department of Materials Science and Engineering, Hanyang University, Seoul 133-791, Republic of Korea*
[c] *BMW Group, Petuelring 130, 80788 Munich, Germany*
[d] *Department of Nano Science and Technology, Sejong University, Seoul, 143-747, Republic of Korea*

† Electronic supplementary information (ESI) available. See DOI: 10.1039/c6ee01134a

‡ Joo Hyung Lee and Chong S. Yoon are co-first authors; they contributed equally to this work.

in this work to maximize the Ni content near the particle core. Among anode materials for LIBs, Si exhibits the highest gravimetric capacity (3579 mA h g^{-1}, when charged to $Li_{15}Si_4$);[10,11] however, a large volume change during cycling often results in pulverization, electrical contact loss, and constant evolution of the solid-electrolyte interphase (SEI), leading to rapid capacity fading.[12,13] One recent trend has been the introduction of various carbon-based nanomaterials such as nanotubes, nanofibers, and graphene into the Si anode because these carbon nanomaterials provide a structural buffer as well as electrically conductive paths.[14–17] The anode strategy proposed in this work is to develop a composite anode consisting of structurally defective Si microparticles encapsulated by carbon nanotubes, fabricated *via* the simple ball-milling of nanoporous Si and carbon nanotubes (CNTs). Here, we show for the first time how high-energy-density Li-ion cells, which meet the target for the mass market introduction of EVs, can be assembled using the combination of the two-slope concentration gradient NCM (TSFCG) cathode, $Li[Ni_{0.85}Co_{0.05}Mn_{0.10}]O_2$ and the CNT–Si composite anode.

2. Experimental

2.1 Material synthesis

Porous Si. Commercially available SiO (325 mesh) from Aldrich was used as the starting material. The thermal disproportionation of SiO was performed in a box furnace at 970 °C for 30 h under Ar/H_2 gas flow (96% Ar, 4% H_2). After heat treatment, the resultant Si/SiO_2 powders were soaked for 4 h in HF solution to eliminate SiO_2. The obtained porous Si was washed with distilled water several times to remove the HF. The washed porous Si was dried in a vacuum oven at 60 °C for 6 h.

CNT–Si. The dried porous Si with CNTs (weight ratio of porous Si : CNT = 85 : 15, K-Nanos 210p Kumho Petrochemical) was introduced with 3 hardened steel balls into a hardened steel vial. The milling process was carried out at 20 Hz frequency for 30 min (15 min + 15 min milling time, with a 20 min break) using a milling machine (MM400, Retsch).

TSFCG $Li[Ni_{0.85}Co_{0.05}Mn_{0.10}]O_2$. To prepare the spherical $[Ni_{0.85}Co_{0.05}Mn_{0.10}](OH)_2$ precursor, the initial Ni-poor aqueous solution (Ni : Co : Mn = 90 : 6 : 4 in molar ratio) from tank 2 composed of $NiSO_4\cdot6H_2O$, $CoSO_4\cdot7H_2O$, and $MnSO_4\cdot5H_2O$ was slowly pumped into a Ni-rich stock solution (Ni : Co : Mn = 100 : 0 : 0 in molar ratio) in tank 1, after which the homogeneously mixed solution was fed into a batch reactor (40 L) filled with a certain amount of deionized water, NH_4OH solution (aq.), and NaOH solution (aq.) in a replenished N_2 atmosphere.[9] Concurrently, a 4.0 mol L^{-1} NaOH solution (aq.) and a NH_4OH chelating agent solution (aq.) were pumped separately into the reactor. In the initial stage of the process, $Ni(OH)_2$ was co-precipitated as a center composition and nickel–cobalt–manganese hydroxides of various compositions were then slowly accumulated onto the formed $Ni(OH)_2$ particles *via* a co-precipitation process. To construct the second concentration gradient layer onto the formed TSFCG hydroxide precursor, an aqueous solution in tank 3 with a Ni-poor concentration (Ni : Co : Mn = 69 : 6 : 25 in molar ratio) was slowly pumped into the mixed solution in tank 1. The precursor powders were obtained through filtering, washing, and drying in a vacuum oven overnight at 100 °C. The obtained TSFCG $[Ni_{0.85}Co_{0.05}Mn_{0.10}](OH)_2$ was mixed with $LiOH\cdot H_2O$ and the mixture was then calcined at 750 °C for 15 h in flowing oxygen.

$Li[Ni_{0.85}Co_{0.11}Al_{0.04}]O_2$ (NCA). For the synthesis of $Li[Ni_{0.80}Co_{0.15}Al_{0.05}]O_2$, the synthesized $[Ni_{0.84}Co_{0.16}](OH)_2$ hydroxide precursor *via* the co-precipitation process was mixed with $LiOH\cdot H_2O$ and $Al(OH)_3\cdot xH_2O$ (Li/(Ni + Co + Al) = 1.01 and Al/(Ni + Co + Al) = 0.04 in molar ratio), and calcined at 750 °C for 10 h in flowing oxygen.

2.2 Analytical techniques

The chemical compositions of the powders were analyzed *via* inductively coupled plasma spectrometry (ICP-MS, NexION 300). The synthesized materials of the crystalline phase were characterized by powder high-resolution X-ray diffraction (HR-XRD, SmartLab, Rigaku) using Cu Kα radiation. XRD data were obtained in the 2θ range between 10 and 80° with a step size of 0.03°. The particle morphologies and structures of all powders were observed by SEM (JSM 6400, JEOL Ltd) and TEM (JEOL 2010, JEOL Ltd). Element mapping was carried out using TEM (JEOL 2100F, JEOL Ltd). To obtain the localized composition of the CNT–Si and TSFCG, cross-sections of the particles were prepared by embedding the particles in an epoxy and grinding them flat. Line scans of the polished surfaces for the TSFCG precursor and the lithiated oxide were determined *via* EPMA (SIMADZU, EPMA-1720). The Brunauer–Emmett–Teller (BET) specific surface area of the samples was determined using an Autosorb-iQ 2ST/MP physisorption analyzer using the standard N2 adsorption and desorption isotherm measurements at 77 K.

2.3 Electrochemical test

CNT–Si half-cell. The working anode was fabricated in a 60 wt% active material, 20 wt% super P carbon, and 20 wt% poly(acrylic acid) (PAA) binder ratio. The obtained slurry was coated onto Cu foil and roll-pressed. The coated electrodes were dried for 6 h at 80 °C in a vacuum oven. The mass loading of the active material was 1.3 mg cm^{-2} and the thickness of the electrode was 16 μm. The electrolyte solution was 1.0 M $LiPF_6$ in ethylene carbonate–diethyl carbonate (EC : DEC, 1 : 1 by vol%) with 10 wt% fluoroethylene carbonate (FEC, TCI). Electrochemical testing was performed in a CR2032 coin-type half-cell adopting Li metal as a counter electrode. The cells were charged and discharged at 30 °C between 0.01 and 1.5 V (*versus* Li^+/Li) by applying a constant 1 C current (8 mA corresponds to 4000 mA g^{-1}).

TSFCG $Li[Ni_{0.85}Co_{0.05}Mn_{0.10}]O_2$ half-cell. The working cathode was fabricated in a 85 wt% prepared powders, 7.5 wt% carbon black, and 7.5 wt% poly(vinylidene fluoride) (PVDF) binder ratio. The obtained slurry was coated onto Al foil and roll-pressed. The electrolyte solution was 1.2 M $LiPF_6$ in ethylene carbonate–ethyl methyl carbonate (EC : EMC, 3 : 7 by vol%). Electrochemical testing was performed in a CR2032 coin-type half-cell adopting Li metal as a counter electrode. The cells were cycled galvanostatically between 2.7 and 4.3 V at 30 °C by applying a constant 0.5 C current (0.9 mA, 1 C current corresponds to 200 mA g^{-1}).

Li-ion full cell. Prior to use in the full cell, the CNT–Si based anode was pre-lithiated for 10 min by pressing it directly against lithium metal wetted by the 1.2 M $LiPF_6$ in ethylene carbonate–ethyl methyl carbonate with 2 vol% vinylene carbonate (VC, TCI). Electrochemical testing was performed in a CR2032 coin-type full cell using the CNT–Si anode, the TSFCG $Li[Ni_{0.85}Co_{0.05}Mn_{0.10}]O_2$ cathode, and 1.2 M $LiPF_6$ in ethylene carbonate–ethyl methyl carbonate with 2 vol% vinylene carbonate electrolyte. The cells were cycled galvanostatically between 2.0 and 4.15 V by applying a constant 1 C current (1.8 mA, 1 C current corresponds to 200 mA g^{-1}) at 30 °C.

3. Results and discussion

3.1 Anode: CNT–Si

The nanoporous Si powder prior to ball milling with CNTs was composed of rather loosely-held agglomerates whose size ranged from 10 to 20 μm. As can be seen in Fig. 1a showing a scanning electron microscopy (SEM) image of the CNT–Si composite anode, high-energy ball milling crushed the nanoporous Si powder to form 2–3 μm-sized agglomerates or secondary particles while narrowing the particle size distribution. The presence of CNTs during ball milling helped to consolidate the individual Si nanoparticles such that each secondary particle after the high-speed ball milling consisted of 200–500 nm-sized Si primary particles. A rough Si surface can be seen in the magnified image in the inset of Fig. 1a, indicating that each Si particle was encapsulated by a network of CNTs. The CNTs were likely also pulverized during ball milling and coated the Si particle surface.[18,19] The SEM image of the cross-section prepared using a focused ion beam (FIB) shown in Fig. 1b confirms that the CNTs were uniformly distributed among the Si particles without visible segregation, as also corroborated by the compositional energy-dispersive X-ray spectroscopy (EDS) mapping shown in Fig. 1c. In agreement with the SEM analysis, the CNT–Si composite anode was an aggregation of CNT-encapsulated Si particles (Fig. 1d); however, it was confirmed by electron diffraction that each individual Si particle was single crystalline (Fig. 1e). Prior to ball milling, the nanoporous Si was a cluster of Si nanoparticles that were ∼20 nm in diameter (see Fig. S1, ESI,† for SEM and TEM images). It appears that the mechanical energy injected *via* ball milling was sufficient to consolidate the Si nanoparticles into a much larger single-crystalline particle. The consolidation of the Si nanoparticles was aided by the fact that melting of the nanoparticles, in general, occurs at a temperature much lower than that of the bulk counterpart.[20] During ball-milling, the presence of CNTs also facilitated the consolidation by minimizing the oxidation and amorphization of the Si nanoparticles by acting as a lubricant and oxygen scavenger.[19] When ball-milled without the CNTs, the Si particles tended to oxidize and grow into a large agglomeration. It is also noted that the non-uniform contrast of the Si microparticle (Fig. 1e) indicates that the particle was highly strained likely due to the structural defects developed during the consolidation of the nanoparticles. Finally, SEM and high-resolution TEM images (Fig. 1f and Fig. S2, ESI†) show the well-developed Si(111) fringes that were covered with a thin layer of CNTs. Therefore, the morphology of the CNT–Si composite anode revealed by Fig. 1 was a rather loosely held cluster of single-crystalline Si particles, of size ranging from 150 nm to 400 nm, which were uniformly covered by CNTs. The encapsulating CNTs should provide efficient electrical paths as well as chemical protection while the loose agglomeration held by mechanically sturdy CNTs should alleviate the mechanical shock and volume expansion associated with the lithiation of the Si anode.

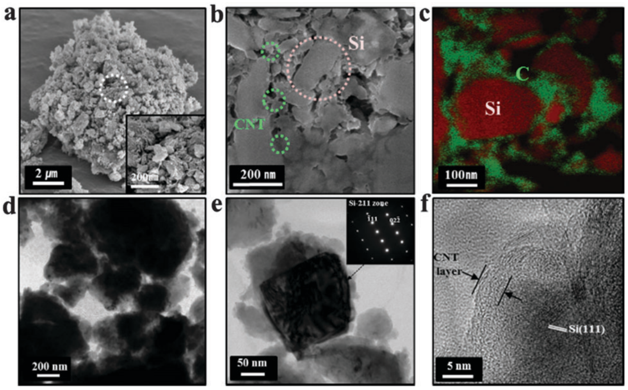

Fig. 1 Structural characterization of the composite CNT–Si anode. (a) SEM image of the single CNT–Si composite particle and high magnification images of marked region (inset). (b) Cross-sectional SEM image of (a). (c) EDS mapping of (a), (d and e) TEM images and SAED pattern (inset) of CNT–Si composite particles. (f) HR-TEM image of the CNT–Si composite particle.

Fig. 2 shows a comprehensive analysis of the electrochemical performance of the CNT–Si composite anode (2032 coin-type

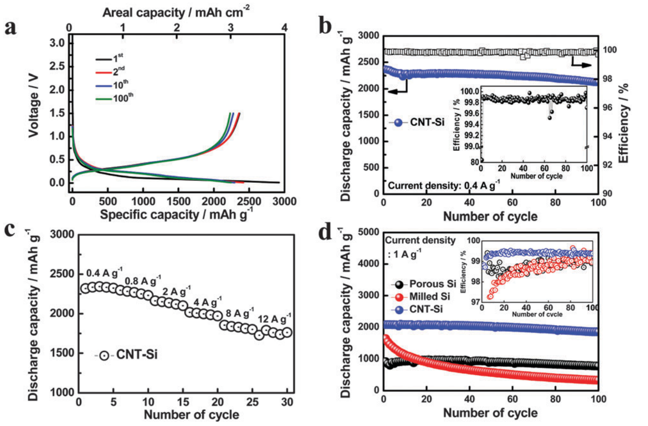

Fig. 2 Charge–discharge characteristics of the CNT–Si composite anode in a half-cell with a Li counter electrode. (a) 1st cycle, 2nd cycle, 10th cycle, and 100th cycle voltage profiles (current density: 400 mA g^{-1} corresponds to 0.1 C). (b) Cycling performance by applying a constant current of 400 mA g^{-1} (0.1 C) and enlarged images of Coulombic efficiency (inset). (c) Rate capability of the composite CNT–Si anode by applying a constant current between 400 mA g^{-1} (0.1 C) and 12 A g^{-1} (3 C). (d) Cycling performance of nanoporous Si and milled Si without CNTs at a current density of 1 A g^{-1} (0.25 C) and enlarged images of Coulombic efficiency (inset). All cells were operated at 30 °C within a voltage range of 0.01–1.5 V.

half-cell tests with a Li counter electrode). Typical voltage profiles of the CNT–Si anode are shown in Fig. 2a (at 400 mA g^{-1}). The CNT–Si anode exhibited an initial discharge (Li^+ extraction) capacity of 2364 mA h g^{-1} with a high initial Coulombic efficiency of 80.8%. After the 1st cycle, however, the Coulombic efficiency reached nearly 100% with minimal drop in the discharge capacity after 100 cycles. The cycling behavior of the CNT–Si composite anode is shown in Fig. 2b, which confirmed the outstanding cycle retention of the composite anode (2130 mA h g^{-1} which is equivalent to 90% of the initial discharge capacity after 100 cycles) while maintaining the Coulombic efficiency of over 99.8%. The inset in Fig. 2b exemplifies the steady Coulombic efficiency of the composite electrode during cycling, resulting from the formation of a SEI layer on the CNT surface.[13,22] The nearly perfect Coulombic efficiency and good capacity retention also proved the mechanical stability of the composite anode being able to accommodate the volume changes during cycling.[21] Moreover, as can be seen in Fig. 2c, the CNT–Si anode demonstrated excellent rate capability at current densities up to 12 A g^{-1}, at which 75% of the capacity at 400 mA g^{-1} was still delivered (1727 mA h g^{-1} at 12 A g^{-1} compared to 2320 mA h g^{-1} at 400 mA g^{-1}). The excellent rate capability of the CNT–Si composite anode is attributed to the efficient electrical conduction paths generated by the network of encapsulating CNTs.

To understand the outstanding cycle retention and Coulombic efficiency exhibited by the CNT–Si composite anode, the cycle performances (at 1 A g^{-1}) of nanoporous Si without CNTs and of bulk Si that was ball-milled without CNTs were compared against the composite anode (Fig. 2d). The cycling data of both nanoporous Si and ball-milled bulk Si without CNTs unequivocally affirmed the benefit of the encapsulating CNTs as the discharge capacity for both electrodes was limited to ∼1000 mA h g^{-1} with an inferior initial Coulombic efficiency of 50–70%. In agreement with the previous results that coating Si with carbonaceous materials such as graphene, CNTs, nanospheres, and carbon film[14,16,17,22–27] greatly improved the overall electrochemical characteristics of the Si anode, the CNT encapsulation protected the Si surface by forming a stable SEI layer, which was confirmed by the impedance spectroscopy measurements shown in Fig. S3 (ESI†). The CNT layer also acted to minimize the stress involved with volume expansion during lithiation[28] which results in rapid capacity drop of milled Si due to structural pulverization.[22,23] The lower specific surface area of the composite anode (111.4 m^2 g^{-1}), when compared to that of nanoporous Si at 350.2 m^2 g^{-1}, is due to consolidation of the Si nanoparticles and leads to a decrease in contact area exposed to the electrolyte, thus reducing the possible electrolyte side reactions and irreversible consumption of Li^+. In addition, structural defects developed within the Si particles (Fig. 1e) during milling partially relieved the strain created *via* Li–Si alloying as it was shown that the structural defects introduced into Si in a controlled manner improved the capacity retention and Coulombic efficiency.[29] Furthermore, the compact nature of the CNT–Si composite anode provided a high tap density of 1.10 g cm^{-3}, as compared to those of other Si-based anodes such as nano-sized Si (0.16 g cm^{-3}),[29] ball-milled micro-sized Si (0.70 g cm^{-3}),[29] and micro-sized Si–C composite (0.78 g cm^{-3}),[30] which can deliver high volumetric energy density of the cell.

3.2 Cathode: TSFCG $Li[Ni_{0.85}Co_{0.05}Mn_{0.10}]O_2$

Inductively coupled plasma (ICP) spectrometry was utilized to obtain the average chemical composition of the TSFCG precursor $[Ni_{0.85}Co_{0.05}Mn_{0.10}](OH)_2$, the final lithiated $Li[Ni_{0.85}Co_{0.05}Mn_{0.10}]O_2$, and the conventional cathode, $Li[Ni_{0.85}Co_{0.11}Al_{0.04}]O_2$ (NCA) (Table S1, ESI†).

Fig. 3a shows a SEM image of a single TSFCG $Li[Ni_{0.85}Co_{0.05}Mn_{0.10}]O_2$ particle. The particle has dense and spherical morphology with an average diameter of 10 μm. A cross-sectional bright field TEM image of the sectioned TSFCG particle (Fig. 3b) shows that the nanorod-shaped primary particles were arranged such that their longitudinal axes were pointing outward from the secondary particle center. In addition, the electron diffraction pattern from a primary particle indexed to the 110 zone in the inset of Fig. 3b affirms that the primary particles have a strong crystallographic texture in which the layered planes were oriented along the radial direction, hence expediting the Li^+ diffusion towards the secondary particle center along the layered planes. It has been well documented that the radial spoke-like morphology combined with the strong crystallographic texture is the defining feature of the compositionally graded cathode that has been synthesized by this laboratory.[5–9] In Fig. 3c, a high-resolution TEM image of a primary particle verified that the (003) planes were indeed aligned in the radial direction. To clarify the compositionally graded structure of the TSFCG cathode prior to cycling, quantitative elemental mapping of Ni, Co, and Mn was carried out on the cross-section sample (Fig. 3d). As designed, the Ni content at the core was maximized using the two-slope approach to deliver the highest possible capacity[9] while the surface was rich in Mn to stabilize the cathode surface. The crux of the two-slope design lies in the edge region (∼1.2 μm thick) where a second Ni compositional gradient was introduced to induce a smooth structural transition from the Ni-rich core to the Ni-deficient surface. Meanwhile, Co maintained a flat gradient to support the rate capability. The mapping result matches well

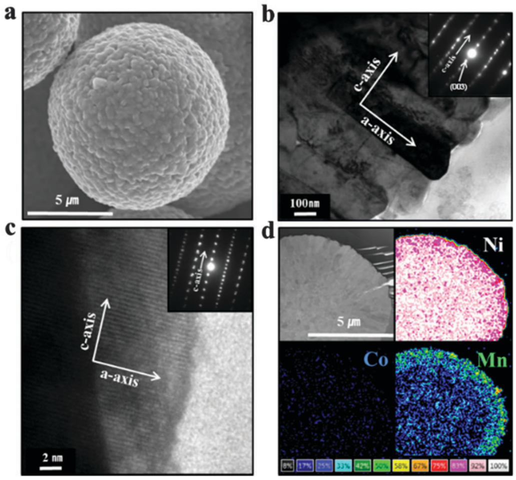

Fig. 3 Structural characterization of the TSFCG cathode. (a) SEM. (b) Cross-sectional TEM and SAED pattern (inset). (c) HR-TEM images and SAED pattern (inset). (d) Cross-sectional EDS mapping of Ni, Co, Mn of the as-prepared TSFCG $Li[Ni_{0.85}Co_{0.05}Mn_{0.15}]O_2$.

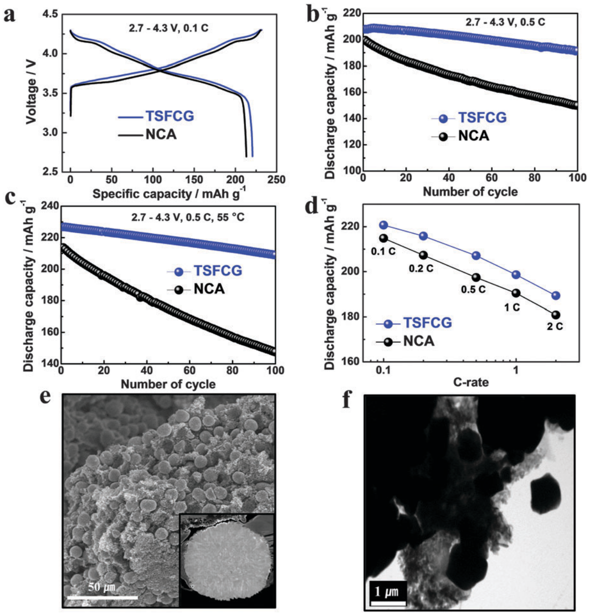

Fig. 4 Electrochemical performance of TSFCG Li[$Ni_{0.85}Co_{0.05}Mn_{0.15}$]$O_2$ and Li[$Ni_{0.85}Co_{0.11}Al_{0.04}$]$O_2$ in a half-cell with the Li counter electrode and characterization of the cycled electrodes. (a) 1st cycle voltage profiles (current density: 20 mA g^{-1} corresponds to 0.1 C). (b) Cycling performance at 0.5 C (100 mA g^{-1}) at 30 °C. (c) Cycling performance at 0.5 C and at 55 °C. (d) Rate capability using a constant current density between 0.1 C (20 mA g^{-1}) and 2 C (400 mA g^{-1}). All cells were operated within a voltage range of 2.7–4.3 V. (e) SEM image and cross sectional SEM image (inset) of TSFCG Li[$Ni_{0.85}Co_{0.05}Mn_{0.15}$]$O_2$ after 100 cycles in a half-cell with the Li counter electrode. (f) Low magnification bright field TEM image of Li[$Ni_{0.85}Co_{0.11}Al_{0.04}$]$O_2$ after 100 cycles in a half-cell with the Li counter electrode.

with the detailed quantitative analysis performed by electron probe micro-analysis (EPMA) (see Fig. S4, ESI†).

Fig. 4 summarizes the electrochemical half-cell performance of the TSFCG Li[$Ni_{0.85}Co_{0.05}Mn_{0.10}$]$O_2$ cathode and compares it with that of a conventional Li[$Ni_{0.85}Co_{0.11}Al_{0.04}$]$O_2$ cathode with equal Ni content. Typical voltage profiles of the TSFCG and NCA cathodes during the first cycle are shown in Fig. 4a at 0.1 C (20 mA g^{-1}) with an upper cutoff voltage of 4.3 V. The TSFCG cathode exhibited an initial discharge (Li^+ insertion) capacity of 221 mA h g^{-1}, which was slightly higher than that of the NCA cathode (213 mA h g^{-1}). However, the benefit of the TSFCG structure becomes clearly noticeable in Fig. 4b as the discharge capacity for the NCA cathode drops markedly during repeated Li-intercalation. Only 75% of the initial capacity was retained after 100 cycles, whereas the TSFCG cathode maintained 92% of its initial capacity. The superior cycle retention of the TSFCG cathode was accentuated in the high-temperature cycle performance at 55 °C (Fig. 4c). In spite of the high temperature, the TSFCG cathode exhibited excellent cycle performance, while the capacity of NCA deteriorated severely. In addition, the rod-shaped primary particles in a spoke-like pattern improved the mobility of the Li^+ ions; hence, the TSFCG cathode showed enhanced rate capability compared to the Ni-enriched NCA cathode. The TSFCG cathode delivered 189.4 mA h g^{-1} at 2 C (400 mA g^{-1}), which is equivalent to 86% of the capacity at 0.1 C (Fig. 4d).

Although the high-resolution XRD analysis of the TSFCG and NCA electrodes in Fig. S5 (ESI†) indicates no development of any secondary phases, the XRD peaks for the NCA electrode after 100 cycles broaden and the lattice parameters calculated from the XRD data indicate cell volume expansion (2.84% for NCA *vs.* 0.43% for TSFCG). On the other hand, no significant structural changes were noticed between the pristine and cycled TSFCG electrodes, suggesting a superior structural stability in comparison with the NCA cathode. The role of the TSFCG structure in maintaining the structural integrity of the electrode during cycling is demonstrated in Fig. 4e, showing a SEM image of the cycled TSFCG cathode. Compared with the pristine particle (Fig. 3a), the spherical morphology was conserved after 100 cycles. A cross-sectional image of the cycled particle in the inset of Fig. 4e contains none of the internal cracks that are typically observed in conventional cathode electrodes, which eventually lead to cathode failure.[31] A high-resolution TEM image of the cycled TSFCG electrode shown in Fig. S6 (ESI†) taken in the 100 zone attests to the structural stability of the TSFCG cathode active material at an atomic scale. A Fourier-filtered image from the marked region shows no structural damage and that the atomic ordering was well maintained even near the surface of the particle. On the other hand, as shown in Fig. 4f, the NCA electrode after 100 cycles was completely pulverized and no traces of the initial morphology were observed, which explains the severe capacity deterioration. A high-resolution image and the Fourier-transformation of the marked regions (Fig. S6b, ESI†) verify the surface damage of the NCA cathode, which developed a NiO-like rock salt phase on the particle surface, similar to the cycled NCA cathodes reported earlier.[32]

To verify the inertness of the TSFCG cathode against electrolyte attack, metal dissolution tests of both electrodes were performed before and after cycling as shown in Fig. S7 (ESI†). Due to the lack of a protective Mn-rich layer at the surface, the Ni dissolution of the NCA cathode was twice as high as that of the TSFCG cathode. In the case of the cycled electrodes, the Ni dissolution of the NCA cathode was three times as high as that of the TSFCG cathode. These structural analyses and metal dissolution tests clearly attest to the superior stability of the TSFCG cathode, enabling the cathode to deliver a high capacity with minimal capacity fading.

3.3 High-energy Li-ion full cells: electrochemical test and post-cycle analysis

A high-energy Li-ion full cell was constructed using the CNT–Si composite anode and the TSFCG Li[$Ni_{0.85}Co_{0.05}Mn_{0.10}$]$O_2$ cathode. In the full cell configuration, vinylene carbonate (VC) was added to the electrolyte to aid the formation of a stable SEI layer on the CNT–Si anode for long term cycling.[33,34] VC instead of FEC, which was used in the half-cell tests of the CNT–Si anode, was chosen because adding FEC to the electrolyte substantially decreased the discharge capacity of the cathode in its half-cell tests (see Fig. S8, ESI†). VC was chosen to optimize the full cell capacity by maximizing the cathode discharge capacity. The pre-lithiation voltage profile of the CNT–Si anode using the VC additive is shown in Fig. S8 (ESI†). Fig. 5a presents typical

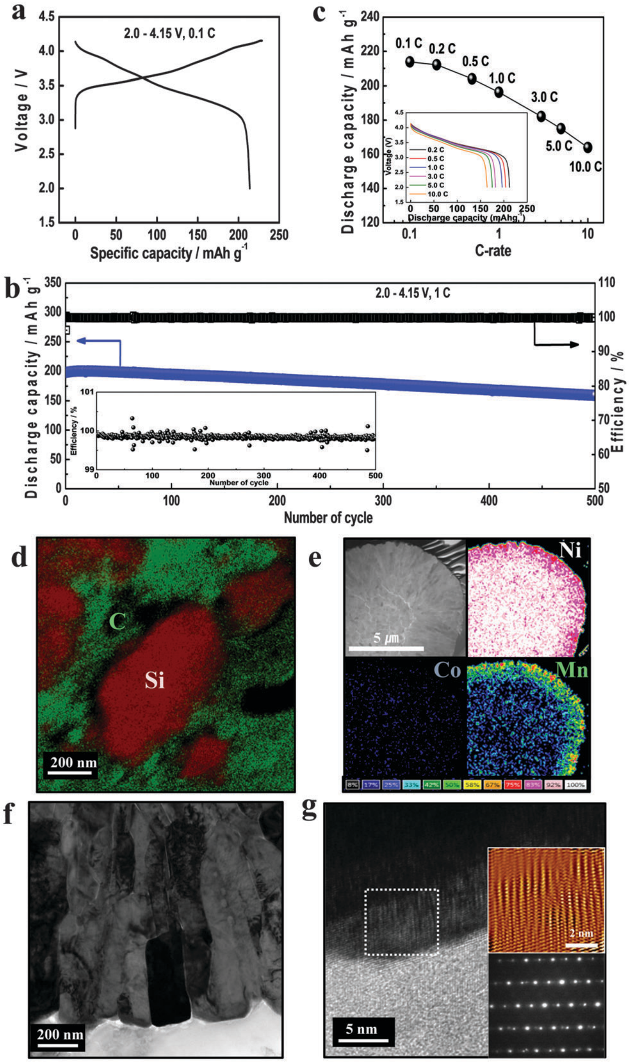

Fig. 5 Full cell performance of the CNT–Si composite anode and TSFCG $Li[Ni_{0.85}Co_{0.05}Mn_{0.15}]O_2$ cathode and characterization of the cycled electrodes. (a) 1st cycle voltage profile at 0.1 C (20 mA g^{-1}). (b) Cycling performance and enlarged images of Coulombic efficiency (inset) at 1 C (200 mA g^{-1}). (c) Rate capability and corresponding discharge voltage profiles (inset) using a constant current density between 0.1 C (20 mA g^{-1}) and 10 C (2 A g^{-1}). All cells were operated at 30 °C within a voltage range of 2.0–4.15 V. (d) Cross-sectional TEM EDS mapping of Si and C in the CNT–Si composite anode after 500 cycles in a full cell configuration with the TSFCG $Li[Ni_{0.85}Co_{0.05}Mn_{0.15}]O_2$ cathode. (e) Cross-sectional EDS mapping of Ni, Co, and Mn, (f) bright field cross-sectional image, and (g) HR-TEM image of TSFCG $Li[Ni_{0.85}Co_{0.05}Mn_{0.15}]O_2$ after 500 cycles including the Fourier-filtered image of the marked region (inset).

1st cycle voltage profiles for the full cell cycled at 0.1 C between 2.0 and 4.15 V. The 1st cycle charge and discharge capacities were 227.8 and 213.0 mA h g^{-1}, respectively, which amounts to 94% of the initial Coulombic efficiency.

The irreversible capacity loss is likely due to the electrolyte decomposition and the formation of the stable SEI layer on the CNT–Si anode. The average working voltage of the battery was 3.63 V, providing a specific energy density of 773 W h kg^{-1} for the TSFCG $Li[Ni_{0.85}Co_{0.05}Mn_{0.10}]O_2$ cathode. Based on the mass fraction analysis of a commercial 18 650 LIB cell,[35] the mass fraction of a cathode active material in a LIB cell is approximately 45% (see Fig. S9, ESI,† for the estimated mass fraction of individual cell components), which translates to a specific energy density of 348 W h kg^{-1} for the CNT–Si/TSFCG cell. This specific energy density of the full cell exceeded the salutary limit imposed by the driving range requirement for EVs.[36] Fig. 5b shows the cycle performance and Coulombic efficiency of the full cell when cycled between 2.0 and 4.15 V at 1 C rate. The CNT–Si/TSFCG full cell delivered 81% of the initial capacity after 500 cycles with an average Coulombic efficiency of 99.8%. The rate capability of the full cell (Fig. 5c) justifies the outstanding rate capability of the CNT–Si/TSFCG full cell which retains 82.7 and 77.5% of the 0.1 capacity at 5 C and 10 C, respectively.

The EDS elemental mapping of the cycled CNT–Si anode from the full-cell after 500 cycles (Fig. 5d) confirmed that there was no noticeable pulverization of the Si particles when compared with the corresponding elemental mapping image of the anode prior to cycling shown in Fig. 1c. The Si particles in the anode remained intact while encapsulated by the CNTs even after 500 cycles. As for the cathode, Fig. S10 (ESI†) compares the compositional profiles of the TSFCG cathodes before and after cycling using EPMA. The two-sloped concentration gradients for Ni and Mn were conserved after 500 cycles. The compositional gradients after 500 cycles are graphically illustrated in Fig. 5e, showing a nearly identical elemental distribution compared to the pristine electrode (Fig. 3d). Even after 500 cycles, a TEM image of the cycled TSFCG cathode (Fig. 5f) also confirms the conservation of the unique, radially aligned nanorod structure. A high-resolution image of the TSFCG electrode after 500 cycles taken in the 110 zone (Fig. 5g) assured that the layered structure was largely maintained although the Fourier-filtered image in the inset suggested local distortion of the transition metal planes. Fig. 5d–g conclusively reaffirm the stability of the CNT–Si/TSFCG full cell during extended cycling while delivering an unprecedentedly high energy density that is suitable for future EVs.

4. Conclusions

In summary, we have designed a fully operational and practical battery system capable of delivering an unprecedentedly high energy density with excellent cycle life using the high-performance CNT–Si composite anode coupled with the TSFCG cathode. A CNT–Si composite anode with high capacity and extremely stable long-term cycling was successfully developed based on the simple ball-milling process. A TSFCG $Li[Ni_{0.85}Co_{0.05}Mn_{0.10}]O_2$ cathode, designed to obtain maximum possible discharge capacity by having a Ni-enriched core and simultaneously ensuring high chemical and thermal stability through an outer Mn-enriched layer, provided a stable Li host structure. The CNT–Si composite anode and the TSFCG cathode in a full cell configuration produced an energy density of 350 W h kg^{-1} with excellent capacity retention for 500 cycles at 1 C rate, satisfying the energy density limit imposed by the range requirement for EVs (see Fig. 6). The proposed battery system integrates state-of-the-art

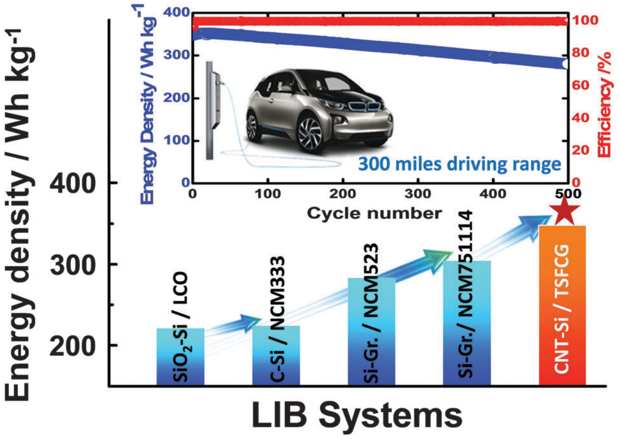

Fig. 6 Energy density of different LIBs. Comparison of the CNT–Si/TSFCG against the currently developed LIBs; LCO: $LiCoO_2$, NCM333: $Li[Ni_{1/3}Co_{1/3}Mn_{1/3}]O_2$, NCM523: $Li[Ni_{0.5}Co_{0.2}Mn_{0.3}]O_2$, NCM751114: $Li[Ni_{0.75}Co_{0.11}Mn_{0.14}]O_2$, and TSFCG: $Li[Ni_{0.85}Co_{0.05}Mn_{0.15}]O_2$. Schematic illustration of Li-rechargeable battery system based on CNT–Si anode and TSFCG cathode for vehicle application (inset).

developments in Li-battery technology to construct a battery delivering an overall electrochemical performance that has not yet been matched to the best of our knowledge. In terms of material costs and synthesis complexity, the proposed battery system is practical and ready to use for energy storage applications that demand high energy, high power, and a long cycle life.

Author contributions

J. H. L. and Y. K. S. conceived and designed the experiments. J. H. L. and J. Y. H. performed material syntheses and electrochemical measurements. C. S. Y. performed TEM experiments and S. J. K., P. L., and S. T. M. characterized electrode active materials. C. S. Y., Y. K. S., S. J. K., and F. M. wrote the paper. All the authors discussed the results and reviewed the manuscript.

Conflicts of interests

The authors declare no competing financial interests.

Acknowledgements

This work was mainly supported by the Global Frontier R&D Program (2013M3A6B1078875) on Center for Hybrid Interface Materials (HIM) funded by the Ministry of Science, Information & Communication Technology (ICT) and the Human Resources Development program (No. 20154010200840) of the Korea Institute of Energy Technology Evaluation and Planning (KETEP) grant funded by the Korea government Ministry of Trade, Industry and Energy. This work was also financially supported by Bayerische Motoren Werke AG (BMW AG).

Notes and references

1 Y. Zhou and T. Stephens, E-Drive Vehicle Sales Analyses, 2014 Vehicle Technologies Annual Merit Review.
2 DoE Annual Merit Review 2012, http://www.anualmeritreview.energy.gov/.
3 D. Andre, *et al.*, *J. Mater. Chem. A*, 2015, **13**, 6709.
4 H. J. Noh, S. J. Yoon, C. S. Yoon and Y. K. Sun, *J. Power Sources*, 2013, **233**, 121.
5 Y. K. Sun, S. T. Myung, M. H. Kim, J. Prakash and K. Amine, *J. Am. Chem. Soc.*, 2015, **127**, 13411.
6 Y. K. Sun, S. T. Myung, B. C. Park, J. Praksah, I. Belharouak and K. Amine, *Nat. Mater.*, 2009, **8**, 320.
7 Y. K. Sun, *et al.*, *Nat. Mater.*, 2012, **11**, 942.
8 H. J. Noh, *et al.*, *Chem. Mater.*, 2013, **25**, 2109.
9 B. B. Lim, *et al.*, *Adv. Funct. Mater.*, 2015, **25**(29), 4673.
10 M. N. Obrovac and L. Christensen, *Electrochem. Solid-State Lett.*, 2004, **7**, A93.
11 S. D. Beattie, D. Larcher, M. Morcrette, B. Simon and J. M. Tarascon, *J. Electrochem. Soc.*, 2008, **155**, A158.
12 H. Wu and Y. Cui, *Nano Today*, 2012, **7**, 414.
13 C. Wang, *et al.*, *Nat. Chem.*, 2013, **5**, 1042.
14 X. Feng, *et al.*, *Nanoscale*, 2014, **6**, 12532.
15 H. Wu, *et al.*, *Nano Lett.*, 2012, **12**, 904.
16 C. Chae, H. J. Noh, J. K. Lee, B. Scrosati and Y. K. Sun, *Adv. Funct. Mater.*, 2014, **24**, 3036.
17 L. Ji and X. Zhang, *Carbon*, 2009, **47**, 3219.
18 B. S. Amirkhiz, *et al.*, *J. Phys. Chem. C*, 2010, **114**, 3265.
19 P. Adelhelm, *et al.*, *J. Mater. Chem.*, 2011, **21**, 2417.
20 M. Zhang, *et al.*, *Phys. Rev. B: Condens. Matter Mater. Phys.*, 2000, **62**, 10548.
21 L. W. Huang, *et al.*, *Int. J. Hydrogen Energy*, 2012, **37**, 1538.
22 H. Wu, *et al.*, *Nat. Nanotechnol.*, 2012, **7**, 310.
23 S. Choi, D. S. Jung and J. W. Choi, *Nano Lett.*, 2014, **14**, 7120.
24 Y. H. Huang, Q. Bao, B. H. Chen and J. G. Duh, *Small*, 2015, **11**, 2314.
25 Y. Cui, *et al.*, *Nano Lett.*, 2012, **12**, 3315.
26 W. Li, *et al.*, *Small*, 2015, **11**, 1345.
27 X. Zhao, C. M. Hayner, M. C. Kung and H. H. Kung, *Adv. Energy Mater.*, 2011, **1**, 1079.
28 L. Xue, *et al.*, *ACS Appl. Mater. Interfaces*, 2013, **5**, 21.
29 M. Gauthier, *et al.*, *Energy Environ. Sci.*, 2013, **6**, 2145.
30 R. Yi, F. Dai, M. L. Gordin, S. Chen and D. Wang, *Adv. Energy Mater.*, 2013, **3**, 295.
31 D. J. Miller, C. Proff, J. G. Wen, D. P. Abraham and J. Bareño, *Adv. Energy Mater.*, 2013, **3**, 1098.
32 S. Watanabe, M. Kinoshita, T. Hosokawa, K. Morigaki and K. Nakura, *J. Power Sources*, 2014, **258**, 210.
33 L. Chen, K. Wang, X. Xie and J. Xie, *J. Power Sources*, 2007, **174**, 538.
34 S. Dalavi, P. Guduru and B. L. Lucht, *J. Electrochem. Soc.*, 2012, **159**, A642.
35 A. W. Golubkov, *et al.*, *RSC Adv.*, 2014, **4**, 3633.
36 D. Andre, *et al.*, *J. Mater. Chem. A*, 2015, **3**, 6709.